Propulsion and Power Research 2021;10(4):317–331

http://ppr.buaa.edu.cn/

Propulsion and Power Research

www.sciencedirect.com

ORIGINAL ARTICLE

Aerodynamic and heat transfer performances of a highly loaded transonic turbine rotor with upstream generic rim seal cavity

Zakaria Mansouri[a,b]

[a]*Faculty of Engineering, The University of Nottingham, Nottingham, United Kingdom*
[b]*ABYLSEN Sciences & Technologies Rhône-Alpes, Grenoble, 38000, France*

Received 27 January 2021; accepted 22 November 2021
Available online 24 December 2021

KEYWORDS

Axial turbine;
Thermal characteristics;
Aerodynamic losses;
Generic cavity;
Purge flow;
Rim seal;
Numerical simulation

Abstract In turbine disk cavity, rim seals are fitted between the stator and its adjacent rotor disk. A coolant air injected through the turbine disk cavity to prevent the ingress of mainstream hot gases. The purpose of this paper is to investigate numerically the effect of the upstream purge flow on the aero and thermal performances of a high pressure turbine rotor. The investigations are conducted on a generic rim seal cavity inspired from a realistic turbofan engine. Four purge fractions (PF) equal to 0.2%, 0.5%, 1.0% and 1.5% of the mainstream are considered. The simulations are done by solving the three-dimensional Reynolds averaged Navier-Stokes and energy transport equations. The results include the effect of the PF on the cooling effectiveness, the sealing effectiveness, the secondary flows with losses and the heat transfer behavior, within the cavity and across the rotor passage. The low PF of 0.2% provided a low cooling effectiveness, a moderate sealing effectiveness and minimum losses. The high PF of 1.5% gave a high cooling effectiveness, a best sealing effectiveness and maximum losses. The medium PF of 1.0% supplied a compromise between the aerodynamic and thermal design needs with good cooling and sealing efficiencies and a tolerable level of losses.

E-mail addresses: mansouri.zakaria@outlook.com, zakaria.mansouri@nottingham.ac.uk.

Peer review under responsibility of Beihang University.

Production and Hosting by Elsevier on behalf of KeAi

https://doi.org/10.1016/j.jppr.2021.11.003

Nomenclature

BL	boundary layer
CFD	computational fluid dynamics
CP	control planes
CRV	counter rotating vortex
CV	corner vortex
GV	geometric vortices
HPT	high pressure turbine
HSV	horse shoe vortex
HTC	heat transfer characteristics
K-H	Kelvin-Helmholtz
LE	leading edge
LV	leakage vortex
MCP	maximum camber point
MSG	mid seal gap
OSG	outer seal gap
PF	purge fractions
PS	pressure side
PV	passage vortex
RANS	Reynolds average Navier-Stokes
RMS	root mean square
SLV	sub-leakage vortex
SRS	scale resolved simulation
SS	suctions side
SV	shear vortices
TE	trailing edge
TKE	turbulent kinetic energy
TPR	total pressure ratio
c	chord (unit: m)
C	constant
cp	heat capacity (unit: J/(kg·K))
H	blade span (unit: m)
h	heat transfer coefficient (unit: W/(m^2·K))
i	incidence angle (unit: degree)
k	turbulent kinetic energy
M	Mach number
m	mass flow rate (unit: kg/s)
Nu	Nusselt number
p	pressure (unit: Pa)
Pr	Prandtl number
q	heat flux (unit: W/m^2)
T	temperature (unit: K)
T^+	normalized near-wall temperature
y^+	normalized first grid cell height

Greek letters

α	flow angle (unit: degree)
β	turning angle (unit: degree)
γ	stager angle (unit: degree)
η	sealing effectiveness
θ	cooling effectiveness
λ	thermal conductivity (unit: W/(m·K))
μ	viscosity of the fluid (unit: Pa·s)
ξ	loss coefficient
ρ	density of the fluid (unit: kg/m^3)
σ	pitch-to-chord ratio
τ	shear stress (unit: Pa)

Subscripts

$+$	non-dimensional near-wall
0	total quantity
1	upstream
2	downstream
∞	freestream
is	isentropic
mix	mixed-out
p	purge flow
s	seal
t	turbulent
w	near wall
x	axial location

1. Introduction

Today's aero-engines run at extreme operating conditions in order to maximize both engine thrust-to-weight ratio and efficiency. Burned gases at the outlet of the combustion chamber and inlet of the turbine reach up the temperatures of 1700 K for commercial aircraft engines and 2200 K for military aircraft engines [1]. Hence, internal cooling, film cooling and sealing technologies become more and more sophisticated to keep up with high gas temperatures requirements. The coolant air is extracted from the compressor in order to cool the hot-gas-path components, such as endwalls, vanes, blades and blade tips, using internal and film cooling, and other hot components, such as turbine disk cavity (wheel-space) using sealing (purged) air. In turbine disk cavity, rim seal is fitted between the stator and its adjacent rotor disk to prevent, or at least, to dilute the ingress of mainstream hot gases to a tolerable level (Figure 1).

It is important to understand the fluid dynamics governing the flow at the periphery of the rim seal. The interaction between the stationary vanes and rotating blades in the mainstream annulus generates an unsteady three-dimensional circumferential pressure asymmetry. Ingress of hot gases occurs in the regions of the clearance where the pressure in the annulus is higher than that in the disk cavity.

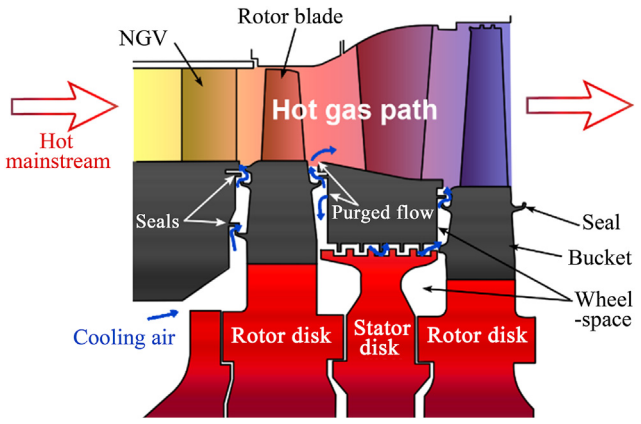

Figure 1 Sketch of multistage turbine secondary-air cooling and sealing.

Egress of purged air occurs in the regions where the pressure difference is reversed [2].

The rim seal performance is explored using both experimental and numerical researches. Experimental researches of academics groups rely widely on turbine cascade test-rigs to investigate the fluid dynamics and heat transfer governing the seal clearance performance. However, turbine cascade rigs do not give a full insight of the ingress and egress phenomenon because they do not always run close to engine operating conditions. Thus, realistic turbine-based rigs running close to engine-operating conditions are more powerful and almost used exclusively in research facilities of aero-engines manufacturers. This kind of rigs is equipped with state-of-the-art instruments of measurements and it is very expensive. Therefore, the numerical researches are the alternative and less expensive approaches to explore the rim seal performance. A very rapid growing trend to use CFD (computational fluid dynamics) codes is raised in industry to design rim seals [3−6] and explore other turbine flows issues [7−10] or even other engine-components issues [11−14].

Regarding the rim seal CFD studies, efforts are focused on many aspects, ranging from the geometric shape of the disk cavity [15−18], going through the physics of the flow and heat transfer characteristics (HTC) within both the cavity [4,19] and hot passages [20,21] and up to the numerical models used for the simulations [6,22]. A survey of recent literature about the different aspects covered in numerical rim seal studies is presented in Table 1. For the geometric shapes of the disk cavity found in the literature, we can classify them in 5 categories, which are: the slot, the basic cavity, the simple cavity, the generic cavity and the realistic cavity. Figure 2 schematizes these different types of cavities. The slot configuration doesn't contain any sealing and it could be inclined or perpendicular to the endwall. The main purpose of using this configuration is to investigate the effect of the purge flow on the aerothermal performance of the rotor passage and the endwall [15,20,23]. The basic cavity contains only one seal and it is usually used to investigate the interaction of the purged flow with the

Table 1 Recent literature survey of the different aspects covered in numerical turbine rim seal studies.

Study	Cavity shape					Focus		Time		Turbulence		Geometry		Motion		Physics	
	Slot	Basic	Simple	Generic	Realistic	Cavity	Passage	Steady	Unsteady	RANS	SRS	NGV	Rotor	Stationary	Rotational	Heat transfer	Flow
Julien et al. [4]					x	x			x	x		x	x		x		x
Jia and Liu [6]			x				x	x		x		x	x		x		x
Popovic and Hodson [21]				x		x	x	x		x			x	x		x	x
Jia et al. [25]			x			x		x		x		x	x		x	x	x
Fiore et al. [26]		x	x			x	x		x		x		x	x			x
Scobie et al. [18]					x	x			x	x		x	x		x	x	x
Wang et al. [16]		x	x			x		x	x	x		x	x		x		x
Cui and Tucker [24]		x					x		x		x		x	x			x
Song et al. [15]	x						x	x		x			x	x		x	x
Song et al. [20]	x						x	x		x			x	x		x	x
Gao et al. [19]				x		x		x	x	x	x			x			x
Zhang et al. [23]	x						x	x		x			x	x		x	x
Ghasemian et al. [17]				x		x		x		x		x	x		x	x	x
Fiore et al. [22]		x	x				x		x		x		x	x			x
Present study				x		x	x	x		x			x	x		x	x

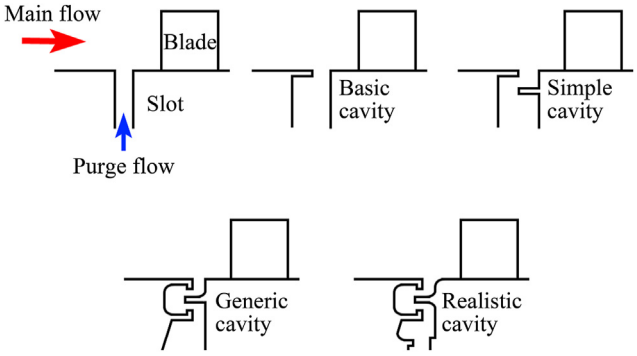

Figure 2 Drawings of different types of disk cavities found in the literature.

mainstream [22,24] using more advanced turbulence models than the Reynolds average Navier-Stokes (RANS) simulation. These models are generally known as the scale resolved simulation (SRS). The simple cavity usually contains two to three superposed seals [6,16]. It is mainly simulated to investigate the effect of the number, shape and position of the seals on the sealing effectiveness. The generic cavity is a more complex type than the above mentioned cavities and its design approaches a lot to aero-engines disk cavities. It could contain several seals, teeth at seals edges, fillets on the corners and variable section passages of the coolant. The generic cavity is simulated to investigate the closest possible representative conditions of the realistic turbine sealing [17,19,21]. The realistic cavity contains more geometric details than the previous type. This kind of cavities is designed by the aero-engines manufacturers and it is studied to improve sealing by geometrical enhancements of a previous version of a realistic cavity or to investigate a new cavity design [4,18] to be included in new aero-engines turbines. In addition to the geometric shapes of the cavities, Table 1 provides other information found in the literature, such as the focus of the studies either in the cavity [4,16,18,21] or in the rotor passage only [6,15,20,24], the physics investigated which concentrates on the flow behavior [4,6,16,24] or both the flow and HTC [15,17,20,23], the turbulence models adopted either RANS [16,18,21] or SRS [19,22,24], the time dependent simulations [18,19,22] or steady ones [15−17], the rotation of the studied domains [4,6,16,18] or not [20−24] and finally the inclusion of the vanes upstream the cavity [4,6,16,18] or not [20−24].

Generally, from the available literature and particularly from the above survey, we can notice the following two main points: 1) The majority of the studies are interested on basic and simple cavities and only few studies investigated generic or realistic cavities. 2) The majority of the studies are focused on the flow and HTC within the cavity or across the hot passage and only very few studies investigated the flow and HTC simultaneously within the cavity and hot passage. To cover this lack, the present study will investigate a generic rim seal cavity inspired from a realistic turbofan engine and it will focus on the flow behavior and

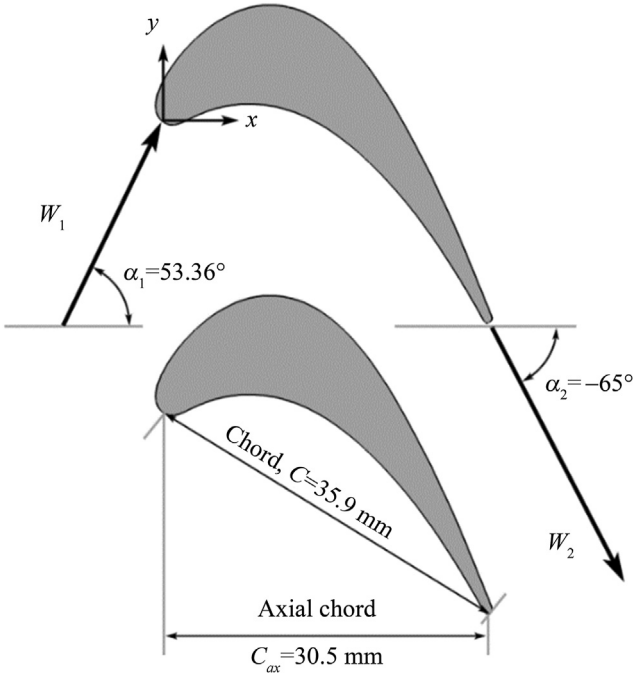

Figure 3 R1S1 turbine rotor geometry nomenclature.

HTC inside the cavity and across the hot passage as well. In addition, this paper will compare a number of purge fractions (PF) to examine the ability of the cavity to prevent ingress of mainstream hot gases as well as to quantify the aerodynamic losses. The effect of the purge fractions on the sealing effectiveness, the cooling effectiveness, the secondary flows with losses and the heat transfer behavior is examined and the results are discussed.

2. Configuration and numerical method

2.1. Rotor blade cascade and generic rim

The present investigation is performed on the two-dimensional high turning rotor blade designated as R1S1. The rotor was designed by SNECMA for modern aero-engines [27,28]. Figure 3 depicts the investigated rotor cascade geometry. The rotor is characterized by a high turning angle of 118.36°, a pitch-to-chord ratio (g/c) of 0.7607 and a stager angle (γ) of 58.38°, while the rest of the geometric parameters and flow conditions are given in Table 2. Several

Table 2 R1S1 high turning rotor details.

Parameter	Value	Unit
Chord (C)	35.9	mm
Axial chord (C_x)	30.5	mm
Pitch-to-chord ratio (σ)	0.7607	−
Blade span (H)	50	mm
Incidence angle (i)	−5	degree
Stager angle (γ)	58.38	degree
Turning angle (β)	118.36	degree

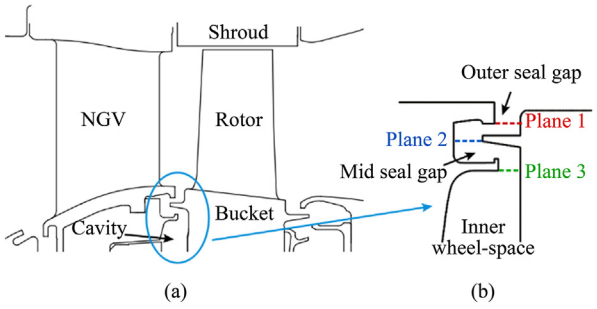

Figure 4 The reference CFM56 HPT cavity (a) and the studied generic cavity (b).

experimental aerodynamic and thermal measurements on this rotor cascade has been done by Arts et al. [29].

Figure 4(a) shows a drawing of the reference design which represents a typical triple seal realistic cavity found in the high pressure turbine (HPT) of the CFM56 turbofan engine. Figure 4(b) shows a drawing of the generic rim seal inspired concept of the disk cavity which is investigated by CFD. The essential difference between the realistic and generic cavity is that the latter features some simplifications, such as removing few fillets from seals corners. The generic cavity features two seals which end with one tooth each at the stator-side and one seal between them at the rotor-side. The choice on using this arrangement of the three seals is to create a guided passage for the cooling air to reduce the penetration of ingress to the cavity. The intention of the two teeth is to provoke a counter-rotating vortex (RCV) to contain the hot ingress.

2.2. Numerical domain, grid and flow conditions

The numerical stationary domain and boundary conditions are shown in Figure 5. The mainstream inlet is located at one axial chord from the rotor leading edge (LE) and the outlet is located at around one and half axial chord from the rotor trailing edge (TE). To reduce computational efforts, only a half of the rotor span is considered and a symmetry condition is imposed at this location. Note that Cui and Tucker [24] found that the midspan region is not affected by the purge flow. A pair of periodic boundaries is imposed at the pitchwise direction so that the numerical domain covers only one blade passage. The rotor-side wall of the cavity is located at around 10% of the axial chord from the rotor LE.

The mesh of the numerical domain is generated in ANSYS-Workbench using multi-block topology and it is shown in Figure 6. The domain is divided into 27 blocks and each block supports a structured mesh. The mesh resolution is very fine and has 6.5×10^6 cells. It is originally generated to support both RANS and SRS calculations. Note that for RANS calculation of a turbomachinery blade passage, a mesh size of 2 million elements is largely sufficient, as it will be shown next. The walls have been resolved using structured boundary layers consisting of 17 elements normal to the passage surfaces and 15 elements normal to the cavity surfaces. The maximum equisize skewness is 0.806 and the maximum y^+ value in order of 1.

The boundary conditions are imposed as following: at the mainstream inlet, a velocity of 70 m/s is imposed with the incidence angle of $-5°$, turbulence intensity of 5% and a hot static temperature of 1473.15 K. At the outlet, a zero Pascal static pressure is imposed with an averaging over the whole surface option. For all the walls, a non-slip and adiabatic conditions are applied. At the cavity inlet, four purge flow rates are investigated which represent fractions from the mainstream mass flow rate, which referred to as the purge fractions (PF = 0.2%, 0.5%, 1.0%, 1.5%). At the same locations, a cooling temperature of 923.15 K is applied with a turbulent length scale equal to this inlet width.

2.3. Numerical parameters and code validation

The simulations are performed using ANSYS-CFX CFD software. The solutions are obtained by solving the 3D steady RANS equations using the finite volume method. The high resolution discretization method is adopted for both the advection scheme and turbulence numerics, which is a second order central difference scheme. The equation of the heat transfer is solved using the thermal energy option. The turbulence model adopted is the two equation k-ω SST with transition formulation (Transition SST) that takes into account the intermittency transport equation similar to Refs.

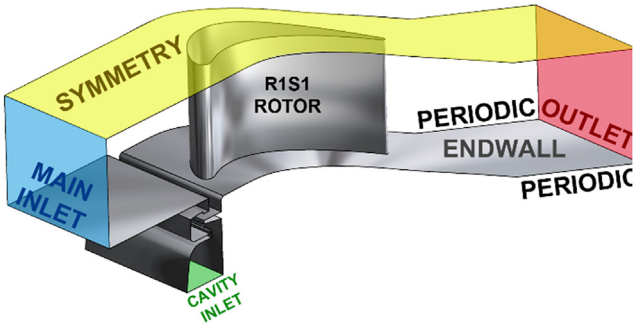

Figure 5 Numerical domain with boundary conditions.

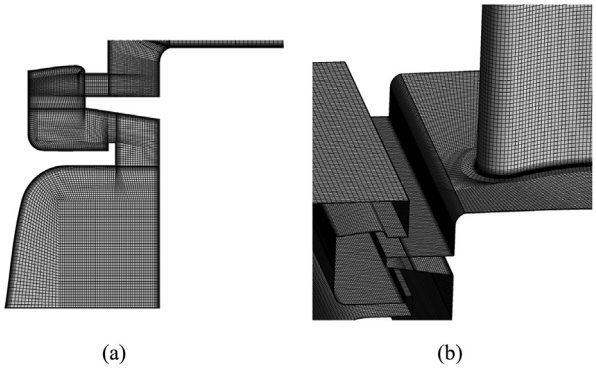

Figure 6 2D mesh of the generic cavity (a) and 3D mesh showing fractions of the cavity, the rotor and the endwall (b).

[9,10]. Note that this steady RANS model is adopted to avoid the huge computational cost of the unsteadiness and the transition formulation can provide comparable results to unsteady RANS.

Various convergence criteria are used, so that the numerical results will be effectively accurate. This is done by checking the static pressure at the rotor surface, the static pressure and the mass flow rate at the outlet of the domain. In addition, the root mean square (RMS) residuals of the mass conservation, the momentum, the energy, the turbulent kinetic energy and the specific rate of dissipation equations are less than 10^{-5}.

To ensure an accurate modeling of the transonic flow across the turbine cascade, a mesh sensitivity study has been conducted. Three different structured meshes of the full span blade were generated in this investigation, which are: coarse mesh of 2 million cells, medium mesh of 3 million cells and fine mesh of 4 million cells. The effect of the mesh refinement on the isentropic Mach number (M_{is}) on the blade surface at mid span 50%, is given in Figure 7. It can be observed that the coarse mesh profile distribution overestimate slightly the shock value (maximum Mach number) comparing with the other meshes and the experimental data. The shock location is at $x/C = 0.82$ and it takes the value of 1.146 for the coarse mesh and 1.12 for the rest of the meshes. Thus, there are no significant differences between the medium and the fine meshes. Moreover, the same cells density of the fine mesh is kept to generate the mesh of the half span blade and the results are given also in Figure 7. It can be seen that the flow in the mid span location is two dimensional without any effects propagating from the endwalls and the result is the same as the full span case.

It is important to check suitability of the numerical method adopted in predicting the thermal behavior on the rotor surface since this study interests in the aero and thermal characteristics of the investigated configuration. Figure 8 shows distributions of the heat transfer coefficient computed with the SST turbulence model with and without transition formulation and compared to experimental data. It can be seen that the blade suction side faces a turbulent/laminar transition of the boundary layer between $x/C = 0.1$ and $x/C = 0.5$. The SST fails to capture this transition,

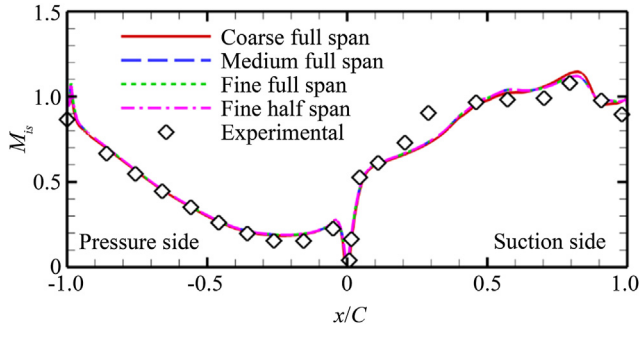

Figure 7 Comparison of different meshes with experimental data of the isentropic Mach number at mid span.

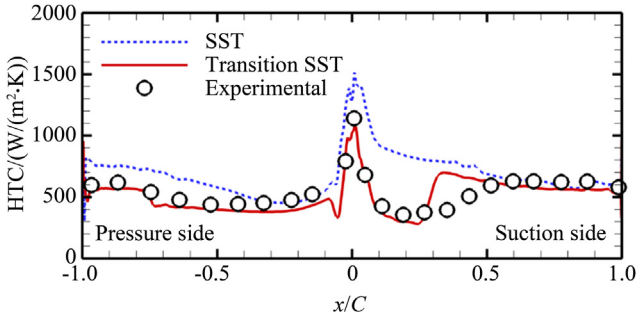

Figure 8 Computation versus experimental data of the heat transfer coefficient at mid span.

whereas the Transition SST model is able to capture it especially between $x/C = 0.1$ and $x/C = 0.3$. At the pressure side, the Transition SST performs better and it reproduces quite well the experimental data. Overall, the validation with the experiments is good for both the isentropic Mach number and the heat transfer coefficient.

3. Results and discussions

3.1. Effects of the purge fractions on the cooling effectiveness

Figure 9 shows contours of the cooling effectiveness θ and 2D streamlines across the mid seal gap (MSG), the outer seal gap (OSG) and near the endwalls of both the stator-side and rotor-side. The cooling effectiveness is given by:

$$\theta = \frac{T_\infty - T}{T_\infty - T_P} \tag{1}$$

Where T_∞ is the temperature of the hot mainstream, T_P is the temperature of the purge flow and T is the local temperature.

These results are plotted at two different axial planes. The first plane in Figure 9(a) locates close to the rotor pressure side (PS) at $-0.1C_x$ following the negative pitchwise direction. The second plane in Figure 9(b) locates near the rotor suctions side (SS) at $0.6C_x$ following the positive pitchwise direction. The location of Figure 9(a) corresponds to the maximum ingress for all PF, where the pressure near the rotor PS above the rim seal is at a maximum value compared to the generic cavity pressure. It can be seen that the counter-rotating vortex is present in the MSG between the toothed stator-side seals as expected. In addition, two kinds of vortices are present in the OSG for all PF. The first kind is the geometric vortices (GV) marked by a black circle (•) which are formed due to the geometric effect on the flow. The GV are located at the vertical stator-side wall and upper corner of the rotor-side seal. The second kind is the shear vortices (SV) which are formed at the OSG due to the mixing of the hot and cold fluids at this flow junction. The lower PF (0.2%) features one SV and the other PF feature two SV. As the PF increases, the size of the vortices

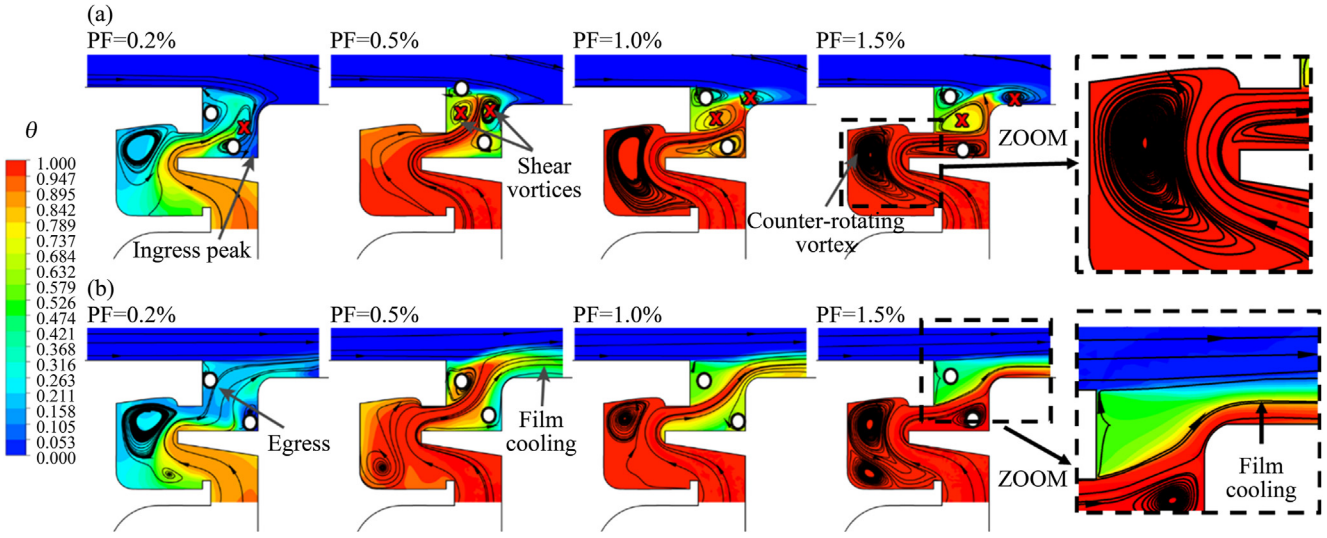

Figure 9 Streamlines and cooling effectiveness within the seal region at maximum ingress (a) and maximum egress (b).

increases also and this is reported to the increase of the PF momentum as its mass flow increases which leads to an ingress resistance by forming more vortices owing to velocity difference across the interface between the two streams. This phenomenon is well known as the Kelvin-Helmholtz (K-H) instability. For the very low PF of 0.2%, the momentum of the cooling fluid is very low, which conducts to a considerable ingress within both the OSG and MSG, where the cooling effectiveness reached its minimum values of 0 at the upper corner of the rotor-side seal and below 0.2 at the OSG. For higher PF (i.e. 1.0% and 1.5%), both SV and CRV are larger and more strength than the ones of the previous low PF and they prevent the ingress from reaching the MSG and limit it only within the OSG. At the upper corner of the rotor-side seal, the minimum θ is about 0.5, 0.82 and 1 for PF = 0.5%, 1.0% and 1.5% respectively. Thus, the formation of more and strength SV leads to more effective sealing. Regarding the θ contours and 2D streamlines of Figure 9(b), they are located at a maximum egress region for all PF. At this region, the pressure around the rotor SS above the rim seal is at a minimum value relative to the pressure of the cavity. It can be noticed that a film of cooling air is formed at the rotor-side endwall and the effectiveness of this film increases as the PF increase. For example, θ reaches its maximum value of 1 for the PF of 1.5% and takes a minimum value of 0.26 for PF = 0.2%. Within the MSG region, the distribution of θ is very similar to the maximum ingress case, where a mixing of hot and cold flows is noticed at PF = 0.2% and a dominant cooling air at PF = 0.5%, 1.0% and 1.5%. For PF = 0.2%, the generated mixing in the maximum ingress region propagates to the maximum egress region within the MSG and with the presence of pressure gradient in favors of the egress, the mixture expelled directly outside the cavity towards the endwall. For the rest of the PF, the high momentum of the cooling air that prevented previously the ingress from reaching the MSG becomes higher in the maximum egress region and is ejected through the OSG directly to the endwall.

Figure 10 shows the aerothermal flow behavior at the endwall, including (a) the cooling effectiveness, (b) surface streamlines and (c) iso-surface of Q-criterion (2×10^7 s^{-2}) for the various PF. From Figure 10(a), the film cooling is restricted to the near rotor SS region for the first three PF (0.2%, 0.5% and 1.0%) and it approaches to the rotor LE for the last PF of 1.5%. As the increase of PF, the purge flow provides a higher effect of cooling on the endwall by injecting more cool air into the film. This is beneficial since it enlarges also the area covered by the coolant (marked by curly brackets). The enlargement of the cooled area is also shown using streamlines in Figure 10(b). After exiting the cavity, the coolant streamlines impinge onto the rotor SS at the maximum camber point (MCP) indicated by a black cross mark. The streamline topology indicates the presence of secondary flow structures at this area. The cooling film is strongly affected by secondary flows, which are shown in Figure 10(c). Several secondary structures can be distinguished, including vortices with large structures and others with small structures. The vortices of large structures in red color are mentioned as the main secondary vortices and they include the leakage vortex (LV), the passage vortex (PV) and the corner vortex (CV). The vortices of small structures are the horse-shoe vortex (HSV) in blue color near the rotor LE and the sub-leakage vortex (SLV) in green color under the legs of the LV. The LV is appeared near the rotor suction side and it is formed due to the interaction between the leakage flow and the mainstream. It is immediately twisted as it approaches to the rotor due to its low momentum compared to the mainstream momentum and to the high camber shape on the rotor suction side. The SLV is the one responsible of generating the red coolant streamlines shown

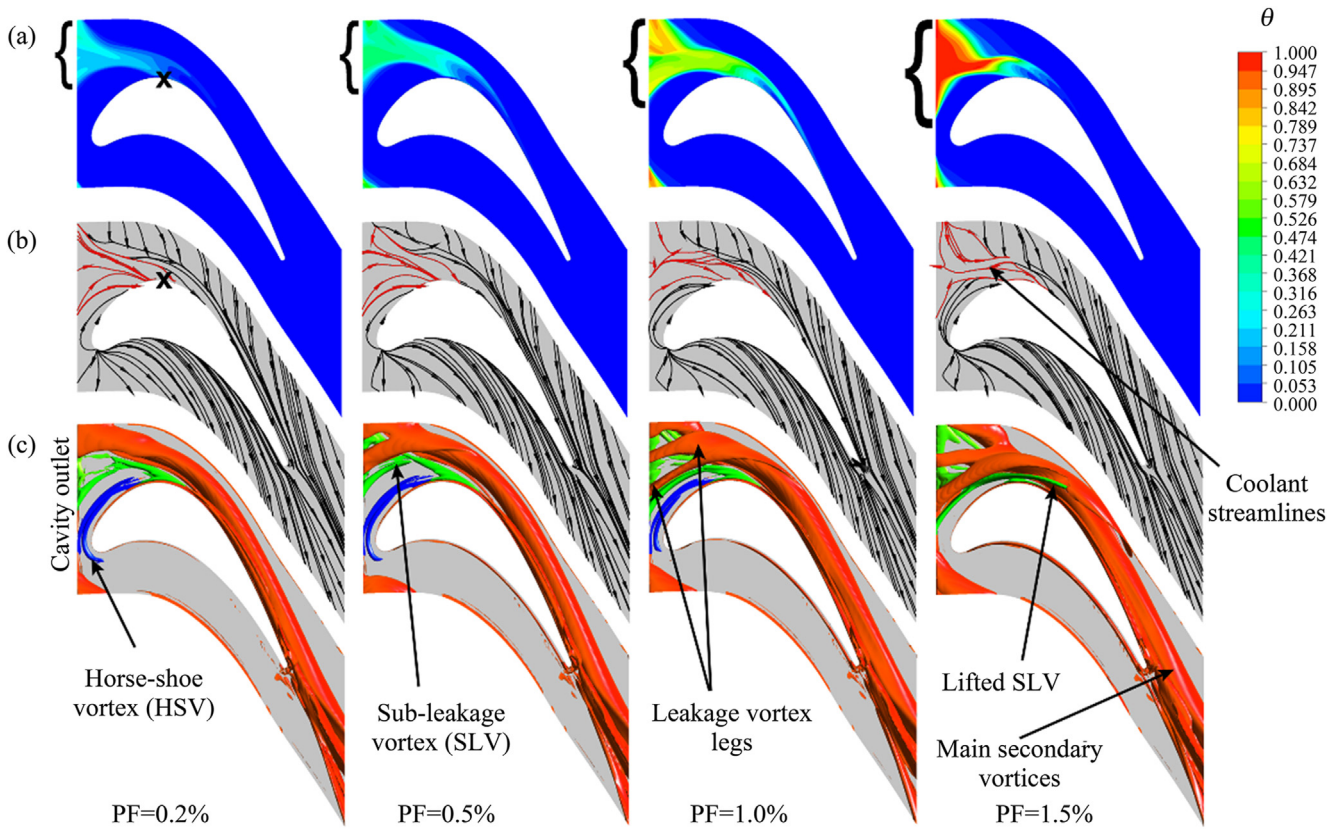

Figure 10 The aerothermal flow behavior at the endwall (a) the cooling effectiveness, (b) surface streamlines and (c) iso-surface of Q-criterion.

in Figure 10(b). It is formed due to the interaction of the leakage flow and the boundary layer of the blade platform (endwall). It has a direct effect on the cooling film since it is in a direct contact with the endwall. The increase of the PF strengthens the SLV and augments its size which brings more coolant and leads to a better effect of cooling. For the first three PF (0.2%, 0.5% and 1.0%), the SLV impinges onto the rotor SS and it collapses downstream the MCP which extends slightly the cooling effect after this point. However, in the highest PF case, the SLV is divided in two structures upstream the MCP. One structure stays in contact with the endwall till it collapses onto the MCP and the other structure it lifts-off and joins the LV due to the very high momentum. Furthermore, the HSV region doesn't contain any cooling effect and its length diminishes as the PF increases till it disappears at PF = 1.5%. As previously said, the increase of PF augments the size of the SLV and as a consequence it narrows the presence region of the HSV and then it suppresses it definitely.

Figure 11 illustrates contours of the cooling effectiveness on the rotor SS for the various PF. At the rotor SS, the overall levels of θ provided by the leakage air are much lower relative to the endwall levels. The high coolant concentration locates on the MCP at the junction between the rotor SS and the endwall where the SLV collapses. After the collision of the SLV, the remained momentum, with its relatively cool mixture, contribute to the formation of the PV. Then, the PV transports the remained relatively cool mixture across the rotor SS since it is in a direct contact with its surface. Note that the LV which contains the highest

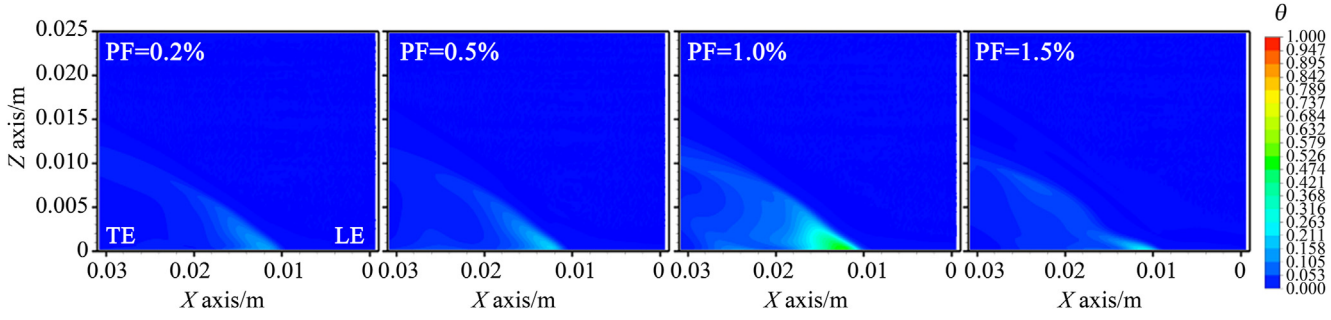

Figure 11 Contours of the cooling effectiveness on the rotor suction side.

levels of the coolant doesn't have any friction with the rotor surface as will be shown in Sections 3.3 and 3.4. Moreover, it can be seen that the increase of PF provides a higher effect of cooling on the rotor SS and this is only valid for the three PF of 0.2%, 0.5% and 1.0%. and not for the highest PF of 1.5%. This is because of the lift-off of the divided SLV structure previously reported in Figure 10(c). The divided structure joined the LV and only a small amount of the SLV contributes to the formation of the PV and consequently to the cooling of the rotor SS.

The maximum cooling effectiveness reached at both the endwall and rotor SS for all PF are shown in Figure 12. At each purge fraction, the maximum θ at the endwall is much higher than at the rotor SS with an absolute difference of 56.4%, 64.6%, 55.0% and 74.0% for the PF of 0.2%, 0.5%, 1.0% and 1.5% respectively. At the endwall, as the PF increases, the maximum θ increases by 40% from PF = 0.2% to PF = 0.5% and 35% from PF = 0.5% to PF = 1.0%. However, θ reaches 1 for PF = 1.0% and 1.5%. At the rotor SS, as the PF increases, the maximum θ increases by 26% from PF = 0.2% to PF = 0.5%, 48.8% from PF = 0.5% to PF = 1.0%. At the highest PF of 1.5%, the maximum θ decreases by 42% compared to the PF of 1.0% due to the small amount of coolant that is in contact with the rotor surface in this case.

3.2. *Effects of the purge fractions on the sealing effectiveness*

Figure 13 shows contours of the sealing effectiveness η_s across the three control planes previously shown in Figure 4. The first plane is located at the OSG and the second plane is located at the MSG and the third plane is located at the outlet of the inner wheel-space. The sealing effectiveness is calculated as follows:

$$\eta_s = \frac{T_\infty - T_s}{T_\infty - T_P} \tag{2}$$

where T_s is the local temperature at the control planes.

In general, the first control plane (CP1) is highly affected by the interaction between the hot mainstream and the purged air due to its location which is characterized by a

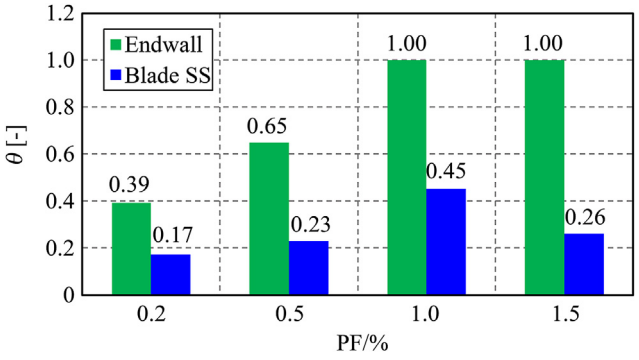

Figure 12 Maximum cooling effectiveness at the endwall and rotor SS.

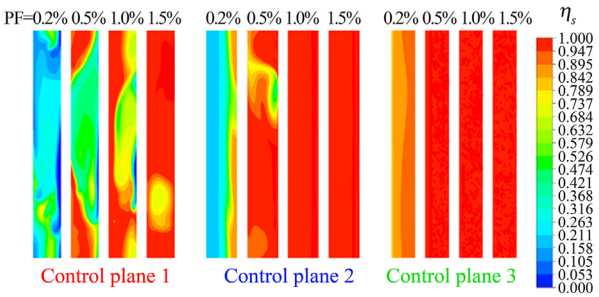

Figure 13 The local sealing effectiveness at different control planes within the generic cavity.

strong shear and heat transfer. The second and third control planes (CP2 and CP3) are less affected by the later interaction. From the CP1, it can be seen that the PF of 1.5% is the most effective one among the other PF. It is previously said that the increase of the coolant mass flow leads to a higher fluid momentum and consequently to lager K-H vortices that resist effectively the ingress. It is important to quantify the area covered by the maximum sealing effectiveness to have an idea about the coolant to mixture ratio at the control planes. The maximum η_s covers 0.0%, 27.13%, 45.82% and 84.43% of the total area of the CP1. This indicates that there is an amount of ingested flow present at this plane for all the PF. From the CP2, it can be noticed that the PF of 1.0% and 1.5% are the most effective among the other PF with a maximum η_s that covers 100% of the total area of the CP2, whereas the PF of 0.2% and 0.5% have 0.0% and 82.82% coverage. From the CP3, it is clearly seen that the PF from 0.5% to 1.5% have a coverage of 100%, whereas the PF of 0.2% still have a zero coverage. Thus, the PF of 0.2% contains only fluid mixture at the three control planes. So, it is hard to quantify the overall sealing effectiveness at the lowest PF using coolant to mixture ratio at each control plane. Moreover, a replacement of the T_s in Eq. (2) by an area-averaged value $T_{s,ave}$ at each control plane is judicious.

The results of the new averaged sealing effectiveness formulation including the area-averaged temperature $T_{s,ave}$ are presented in Figure 14. The highest PF of 1.5% can be

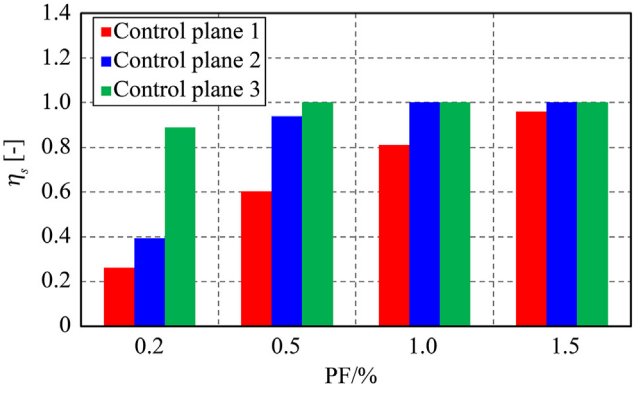

Figure 14 The averaged sealing effectiveness for the different control planes.

seen to exhibit the best averaged η_s for the control planes. The averaged η_s is 1 at CP2 and CP3 respectively, so, the hot mainstream is not present at these locations. At CP1, the averaged η_s is equal to 0.96, so, there is a small amount of ingested flow present at this plane. The PF of 1.0% can be seen to exhibit the best averaged sealing effectiveness for both CP2 and CP3 with $\eta_s = 1$, but for the CP1, the averaged η_s is 0.81. For the PF = 0.5%, the best averaged η_s is at CP3 ($\eta_s = 1$), whereas at CP2 and CP1 it is equal to 0.93 and 0.6, respectively. The lowest PF of 0.2% can be shown to exhibit the worst averaged sealing effectiveness for CP1 and CP2. The averaged η_s is equal to 0.88, 0.39 and 0.26 at CP3, CP2 and CP1, respectively. Thus, the generic cavity reaches a good sealing performance only at the third seal near CP3. Furthermore, one important information that should be noticed also from Figure 14 is the growth rate of the averaged η_s from CP3 to CP1 at each PF. It represents the absolute difference of the averaged η_s between CP3 and CP1 and takes the values of 70.45%, 40%, 19% and 4% from the lowest to the highest PF respectively. This result shows that the growth rate of η_s becomes considerable as the PF decreases and the third seal near CP3 prevents in a successful way the ingress even at the lowest PF. Finally, from the thermal design point of view, the best PF case is the one with the highest sealing performance (PF = 1.5%). However, the aerodynamic design needs should be also checked to see if the amount of losses that could be generated using this PF is acceptable or not.

3.3. Effects of the purge fractions on the secondary flows and losses

Figure 15 reveals all the secondary flows present in the investigated rotor cascade which are visualized using the Q-criterion. As previously mentioned in Section 3.1, various secondary structures can be distinguished with different sizes and shapes. These structures are described from upstream to downstream as the following: Kelvin-Helmholtz structures (in yellow color) are present around the OSR and they are developed due to the interaction between the hot mainstream and the purged air. The velocity difference between the two streams promotes the development of a shear layer with a rolling up process and consequently vortical rolling structures are generated. The SLV (in green color) is extended from the cavity outlet to the rotor SS region across the endwall. It is produced as a result of the combination of the purge flow and the endwall boundary layer under the effect of blade suction. The HSV (in blue color) is formed in front of the rotor LE due to the obstruction of flow by this later which results in a stagnation line. The LV (in red color) is the largest secondary flow among the others which comes out from the cavity near the rotor SS as an egress. The LV has leg-structures which are strongly affected by the purge flow rate. The low PF of 0.2% features one leg, the PF of 0.5% exhibits two legs and the PF of 1.0% and 1.5% feature three legs each. The increase of the number of the leg-structures from the low to high PF is due to the increase of the momentum of the cooling fluid. The leg-structures phenomenon is also reported by Zhang et al. [30]. After its exit from the cavity, the LV it is immediately transported by the mainstream through the rotor passage and swept downstream. The PV (in purple color) is the second dominant flow structure after the LV. For the cases of blade cascades without rim seal cavity, the passage vortex originates from the momentum deficit of the endwall boundary layer after meeting the rotor SS [24]. For the present case with the generic cavity, the combined SLV and endwall boundary experience a pitchwise adverse

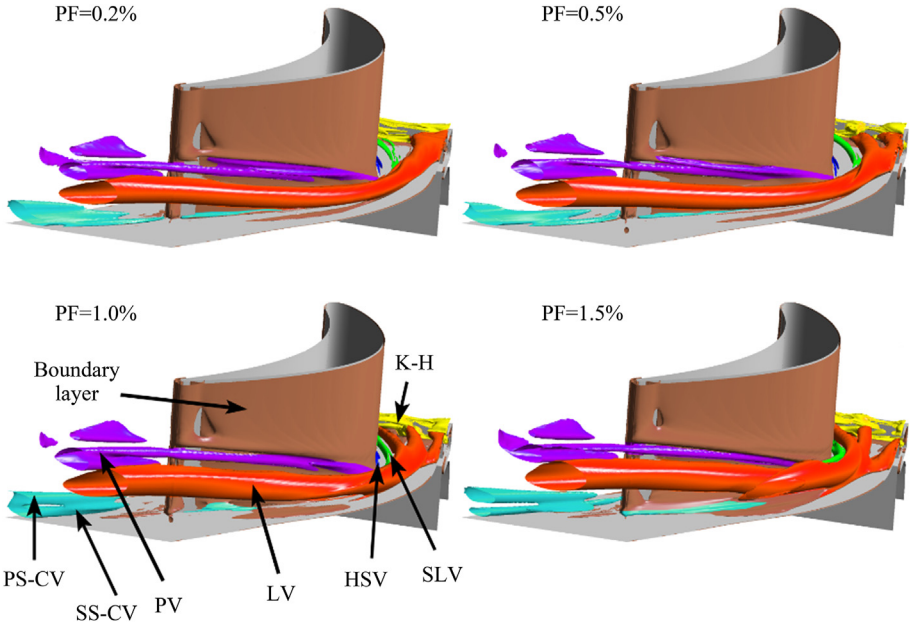

Figure 15 The secondary flows visualized using the Q-criterion.

pressure gradient as they approach to the MCP. The low momentum flow within this region starts to interact with the boundary layer of the rotor SS and they roll up into a PV. The last secondary flow is the CV (in cyan color) which is formed at the junction of the rotor and endwall in both suction and pressure sides. It is produced under the effect of the transverse pressure gradient toward the endwall [31]. The SS-CV and PS-CV are joined downstream the rotor TE to from a single structure at the PF of 0.2% and 0.5%, two structures at PF = 1.0% and 1.5%.

From one hand, it is interesting to see the strength of each of the dominant vortices downstream the rotor. Figure 16 illustrates the contours of the Q-criterion at (y-z) plane downstream the rotor at $0.3C_x$ from the TE. Both the LV and PV exhibit the highest rotational intensity compared to the CV. The LV has the largest shape; the PV features a double detached structures above and the CV become more strength and separated as the PF increases. Note that the dominant vortices are associated to a strong entrainment and mixing effects that induce pressure losses. To investigate these losses, total pressure ratio (TPR) contours are plotted the same pervious plane in Figure 17. The TPR represents the local total pressure normalized by the inlet total pressure value. Near the endwall, areas of low pressure can be observed due to the boundary layer. This later is connected to the CV, where its low pressure levels are extended to the vortex. The increase of the PF leads to lower pressure levels within the CV which means more losses. Out of the endwall, the majority of the losses are related to the dominant leakage and passage vortices. In addition, a wake occurs downstream the rotor TE above the PV and contributes also to pressure losses.

From the other hand, it is very important to quantify the amount of pressure loss at each PF. The losses are expressed as a coefficient relative to a baseline cascade configuration without cavity (flat endwall), similar to Popovic and Hodson [21]. The baseline loss coefficient is calculated as follows:

$$\xi_{baseline} = \frac{p_{01} - p_{02,mix}}{p_{01} - p_2} \tag{3}$$

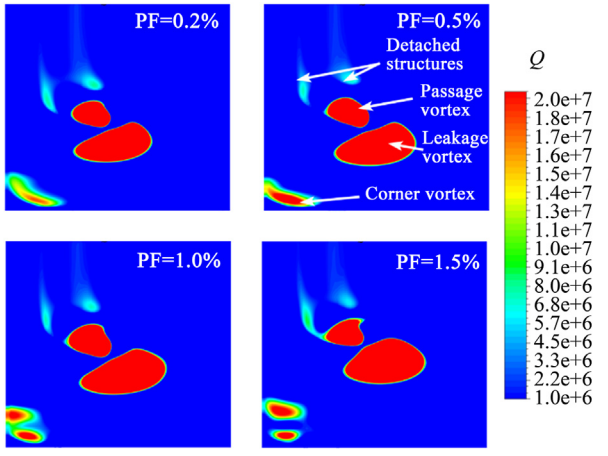

Figure 16 Contours of the Q-criterion showing the intensity of the secondary vortices.

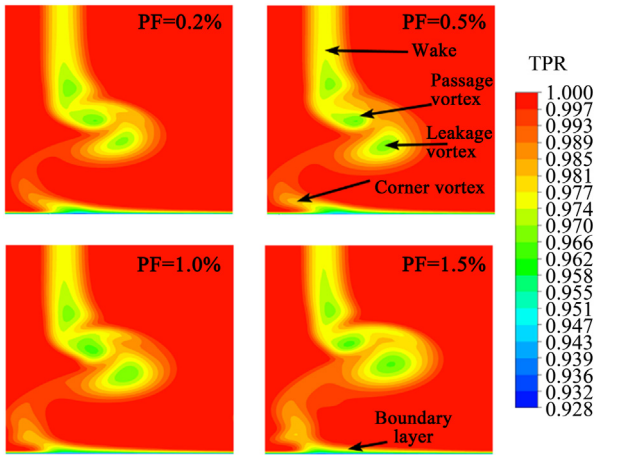

Figure 17 Contours of the losses induced by the dominant vortices.

where p_{01} is the inlet total pressure of the hot mainstream and $p_{02,mix}$ and p_2 are the mixed-out total pressure and static pressure downstream the rotor TE, respectively.

The generic rim seal loss coefficient is given by:

$$\xi_{purge} = \frac{p_{01,eff} - p_{02,mix}}{p_{01} - p_2} \tag{4}$$

where $P_{01,eff}$ is the effective total pressure at the inlet and it is given by:

$$p_{01,eff} = \frac{\dot{m}_\infty p_{01} + \dot{m}_P p_{0,cav}}{\dot{m}_\infty + \dot{m}_P} \tag{5}$$

where $p_{0,cav}$ is the total pressure at the cavity inlet (see Figure 4) and $\dot{m}_\infty$ and $\dot{m}_P$ are the mass flow rates of the mainstream and purge flow, respectively.

Finally, the relative loss coefficient is:

$$\xi_{relative} = \xi_{purge} - \xi_{baseline} \tag{6}$$

Figure 18 shows the relative loss coefficient at each PF. In general, the losses increase when the PF increases as expected and this is due to the increase of the viscous effect within the vortices and the higher friction near the endwall. The evolution of the losses is non-linear. They increase from the lowest PF to the next and so on by 17.85%, 10.82% and

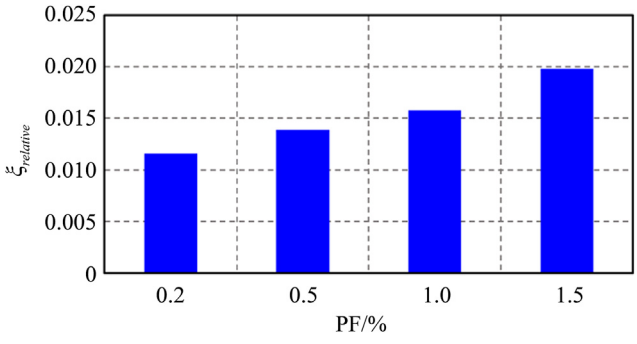

Figure 18 Relative aerodynamic losses for the investigated purged fractions.

20.7% respectively. From the aerodynamic design point of view, the best PF case is the one with the smallest losses (PF = 0.2%). However, this choice is confronted to the thermal design needs to keep the wheel-space at acceptable temperature, which is not reached with the PF of 0.2% for the present study. Moreover, the final choice that will give a compromise between the aerodynamic design and thermal design needs will be discussed in the conclusion.

3.4. *Effects of the purge fractions on the heat transfer behavior*

Figure 19 depicts the Nusselt number (*Nu*) distributions on the rotor SS under the effects of the secondary flows for all the PF. It shows also an iso-value (black line) of the Q-criterion at three different axial chord locations (C_x = 30%, 60% and 90%) to visualize the boundary layer thickness and the secondary vortices. The Nusselt number is calculated as follows:

$$Nu = \frac{hC_x}{\lambda} \tag{7}$$

where h is the convective heat transfer coefficient and λ is the thermal conductivity of the fluid.

The heat transfer coefficient is derived from the near wall heat flux q_w equation as follows:

$$q_w = h\Delta T = \rho \cdot cp \cdot \frac{u^*}{T^+}\Delta T \tag{8}$$

where ρ and cp are the fluid density and heat capacity respectively, u^* is the velocity scale in the logarithmic region of the boundary layer and it represents the viscous term and T^+ is the non-dimensional near-wall temperature and it represents the thermal term. ΔT is the temperature difference between the wall and the fluid. The velocity u^* is proportional to a constant $C_\mu = 0.09$ and the turbulent kinetic energy (TKE) k. The TKE is proportional to the shear stress τ and the turbulent viscosity μ_t. The temperature T^+ is a function of Prandtl number Pr and a non-dimensional near wall grid distance y^*. The full details of the formulations of these quantities could be found in Ref. [32].

Around the midspan region (H = 50%) and following the streamwise direction, the boundary layer (BL) developed exhibits an increasing thickness. This behavior is due to the turning of the rotor geometry. When the mainstream

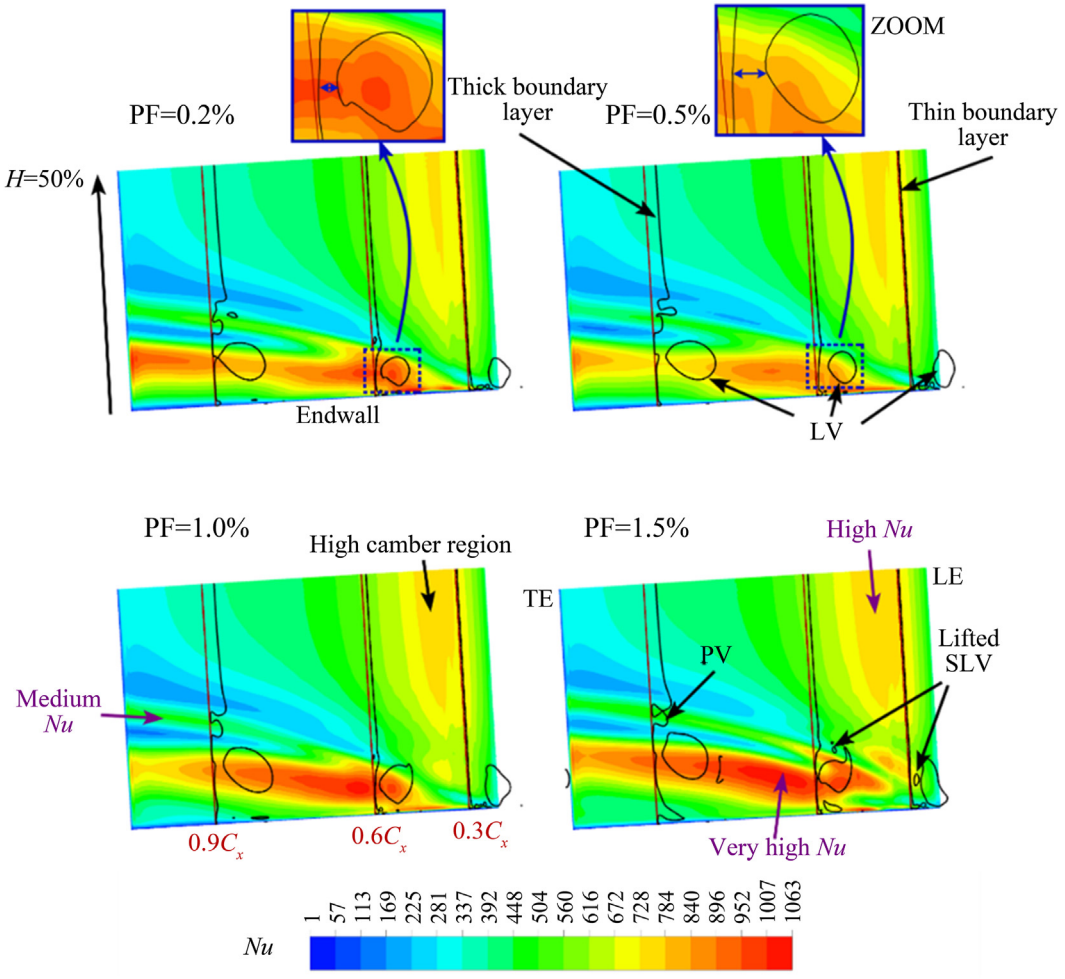

Figure 19 Contours of Nusselt number at the rotor SS for the different PF.

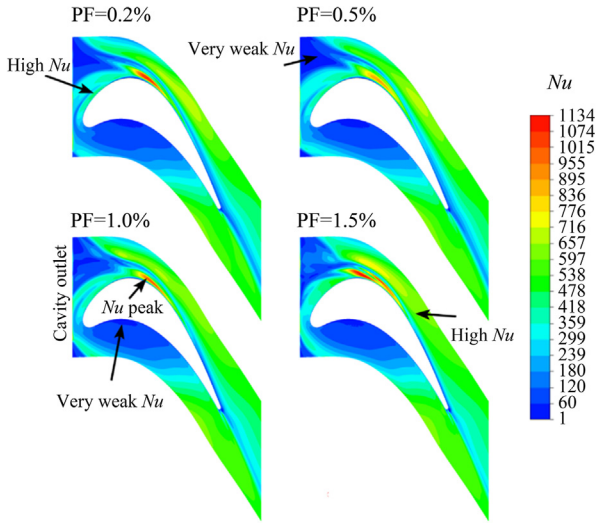

Figure 20 Contours of *Nu* at the endwall for the different PF.

passes through the rotor, it accelerates from the LE to the high camber region, where it reaches its maximum speed, and during this, the production of the TKE increases under the effect of the high flow shear leading to a thin BL. Downstream the high camber region, the flow decelerates and the dissipation of the TKE within the BL takes place leading to a thick BL. The thin BL induces a high heat transfer (a high *Nu*) and the thick BL induces a weak *Nu*. The mechanism behind this, is that the thin BL contains a high shear stress τ which is proportional to the TKE in the eddy-viscosity turbulence models ($\tau = f(k)$ so, high τ gives high k). Hence, the increase in the TKE affects directly the viscous term u^* in Eq. (8) to be much higher than the thermal term T^+ and consequently it induces an increase in h. Far from the midspan and towards the endwall, the *Nu* forms high variation at different locations due to the presence of the secondary flows, similar to the findings of Shih and Yang [1]. They reported that large local variations in heat transfer often result from vortices of varying intensities scouring the walls of the turbine passage. A very high heat transfer starts from the high camber region (near the endwall) to downstream is induced by the LV. At this region the rotor BL is considerably influenced by the LV that turned it thinner. Not that the LV is not in a direct contact with the rotor surface. The viscous energy transfer between the LV and the BL promotes a very high shear stress and consequently a very high *Nu* in this region. It is previously said that the increase in PF flow rate results in higher momentum within the LV and higher size. Consequently, the increase in the LV momentum results in a higher heat transfer. Thus, as the PF increases, the *Nu* increases near the LV region except for the PF of 0.5%. It has the lowest value of the maximum *Nu* among the other PF. Note that the maximum *Nu* at the rotor SS is: Nu_{max} = 970, 962, 1046 and 1053 for PF = 0.2%, 0.5%, 1.0% and 1.5%, respectively. The decrease of the Nu_{max} at the PF of 0.5% is due to the distance between the LV and the BL which is relatively large compared to other PF cases. A zoom near the LV region at $0.6C_x$ indicates this large distance (the double head blue arrow) at PF = 0.5% compared to a smaller distance at PF = 0.2%. Moreover, with this relatively large distance, the BL is less influenced by the LV and the *Nu* levels are slightly low compared to the *Nu* levels of the other PF cases. A medium *Nu* streak is formed above the very high *Nu* region and it is almost parallel to this later. The medium *Nu* streak is induced by the PV that is merged with BL layer. At this location, the BL is highly corrugated due to the mixing process of the PV, which is in direct contact with the rotor SS. The momentum within the PV and its size are lower than in the LV ones. This promotes less viscous energy transfer and consequently less heat transfer in this region.

Figure 20 shows the contours of *Nu* on the rotor endwall for all the PF. The endwall exhibits large local variations in Nusselt number similar to the rotor SS. The endwall could be divided in regions with a very low heat transfer (very weak $Nu \leq 100$) and regions of high *Nu*. The regions of the very weak *Nu* are mainly located around the rotor PS region and at the near rotor SS region in front of the cavity outlet where the film cooling is present. In the first location, there are no vortices scouring the endwall. However, in the second location, the SLV is present and it is merged with the endwall BL as previously reported. The SLV should have caused a high heat transfer in this region, but it didn't happen. The reason is that this region is covered by the cooling film which contributes to considerably increase the thermal term T^+ of Eq. (8) to be much higher than the viscous term u^* and consequently it induces a drastic increase in h. The regions of the high *Nu* are mainly located around the rotor LE, the MCP and downstream near the rotor SS. The LE region experiences high heat transfer because of the roll-up of the horseshoe vortex, similar to Song et al. [15,20]. The MCP region experiences much higher heat transfer with *Nu* peaks due to the impinge of the coolant onto the rotor SS and results a strong recirculation (high flow shear). Note that Shih and Yang [1] mentioned that the heat transfer and secondary flow phenomena in the throat region (MCP) are complex and apparently depend on incoming boundary layer thickness. The downstream area near the rotor SS is composed also of high *Nu*. After the lift-off of the LV, with its complex structure that evolves from one to three legs as the PF increases, a new BL driven by the cross-passage pressure gradient is formed. The new BL fed on the remained shear flow of the LV. The heat transfer rates in this region are slightly higher than those of the LE.

4. Conclusions

A computational investigation is conducted to investigate a turbine rotor cascade with a generic rim seal cavity inspired from a realistic turbofan engine. The flow behavior and heat transfer characteristics within the cavity and across the hot passage are analyzed in details. Calculations are done for different coolant fractions and the ability of the

cavity to prevent ingress of the hot mainstream gases is assessed and the losses are quantified as well. The conclusions from the discussed results are drawn as follow:

1) The cooling effectiveness is examined at two critical locations within the cavity. The first location corresponds to the maximum ingress and contains geometric and shear vortices that resisted the ingress. The second location corresponds to the maximum egress, where a cooling film came out from the cavity and covered the rotor endwall. The rotor surface is less affected by the cooling film compared to the endwall.
2) The sealing effectiveness across three control planes inside the cavity is assessed. The highest PF of 1.5% showed the best averaged sealing effectiveness at all the considered planes. However, the best sealing performance is reached at the inner wheel-space plane by PF = 0.5%, 1.0% and 1.5%. The lowest PF of 0.2% exhibited the lowest sealing performance at all the planes.
3) The secondary structures within the cascade are investigated and they include: Kelvin-Helmholtz structures, sub-leakage vortex, horse-shoe vortex, leakage vortex, passage vortex and corner vortex. The analysis revealed that the secondary vortices are associated to a strong entrainment and mixing effects that induce pressure losses. The losses are increased when the PF is increased as expected and it was due to the increase of the vortices intensity.
4) The heat transfer rates are investigated using the Nusselt number distributions on both the rotor suction side and endwall. The upper rotor surface featured a boundary layer with an increased thickness in the streamwise direction due to the rotor turning. Thin BL induced high *Nu* and thick BL induced low *Nu.* The lower rotor surface featured a BL strongly influenced by the leakage and passage vortices that generated high levels of *Nu.*

As a general conclusion, an optimum purge flow rate should be chosen among the investigated fractions. This choice should respect a compromise between the aerodynamic and thermal design needs. Although the purged flows should be typically minimized to reduce the penalties on the engine performance, the minimum PF of 0.2% does not prevent the ingress of the hot mainstream. An excess of the supplied flow can prevent the ingestion effectively and maintain the generic cavity at a cool temperature, but the maximum PF of 1.5% generates unacceptable pressure losses. In aero-engines design, the disk cavities are supplied with extra margins of coolant to avoid probabilities of seals deteriorations or other failure scenarios. Thus, in the present study the PF of 1.0% is selected as an optimum choice since it respects the extra margins design condition compared to the PF of 0.5% and it has a tolerable level of losses.

Acknowledgements

The author is thankful to Dr. A. Settar from the French National Institute of Applied Sciences (INSA Centre Val de Loire) for the technical support, the discussions and his helpful comments.

References

[1] T.I.-P. Shih, V. Yang, Turbine Aerodynamics, Heat Transfer, Materials, and Mechanics, American Institute of Aeronautics and Astronautics, 2014.
[2] J.W. Chew, T. Green, A.B. Turner, Rim Sealing of Rotor-Stator Wheelspaces in the Presence of External Flow, ASME Paper No. 94-GT-126, 1994.
[3] D. Bohn, M. Wolff, Improved formulation to determine minimum sealing flow − $C_{w,min}$ − for different sealing configurations, ASME Paper No. GT2003-38465, 2003.
[4] S. Julien, J. Lefrancois, G. Dumas, G. Boutet-Blais, S. Lapointe, J.-F. Caron, Simulations of Flow Ingestion and Related Structures in a Turbine Disk Cavity, ASME Paper No. GT2010-22729, 2010.
[5] I. Popovic, H.P. Hodson, Improving turbine stage efficiency and sealing effectiveness through modifications of the rim seal geometry, ASME J. Turbomachinery 135 (2013) 061016-1−061016-10.
[6] W. Jia, H.X. Liu, Numerical investigation of the effect of rim seal on turbine aerodynamic design parameters and end wall flows in low-aspect ratio turbine, Comput. Fluids 74 (2013) 114−125.
[7] Z. Mansouri, A. Settar, H. Khamane, Computational investigation of heat load and secondary flows near tip region in a transonic turbine rotor with moving shroud, Appl. Therm. Eng. 136 (2018) 141−151.
[8] H. Khamane, A. Azzi, Z. Mansouri, Numerical investigation of film-cooling effectiveness downstream of a micro ramp, Comput. Therm. Sci.: Int. J. 10 (2018) 151−165.
[9] Z. Mansouri, Unsteady simulation of flow and heat transfer in a transonic turbine stage under non-uniform inlet conditions, Int. Commun. Heat Mass Tran. 129 (2021) 105660.
[10] Z. Mansouri, Numerical prediction of heat transfer characteristics on a turbine nozzle guide vane under various combustor exit hot-streaks, Heat Transfer 51 (2022) 976−997.
[11] H. Djedai, M. Ramzi, Z. Mansouri, A. Mokhtar, Numerical investigation of three-dimensional separation control in an axial compressor cascade, Int. J. Heat Technol 35 (2017) 657−662.
[12] Z. Mansouri, T. Boushaki, Investigation of large-scale structures of annular swirling jet in a non-premixed burner using delayed detached eddy simulation, Int. J. Heat Fluid Flow 77 (2019) 217−231.
[13] Z. Mansouri, T. Boushaki, M. Aouissi, I. Gökalp, Computational investigation of a swirled premixed burner using hybrid RANS-LES method, Notes on Numerical Fluid Mechanics and Multidiskiplinary Design 137 (2018) 243−254.
[14] Z. Mansouri, T. Boushaki, M. Aouissi, Detached eddy simulation of non-reacting swirling flow in a vortex burner, Int. J. Heat Technol. 35 (2017) 594−602.
[15] L.M. Song, P.Y. Zhu, J. Li, Z.P. Feng, Effect of purge flow on endwall flow and heat transfer characteristics of a gas turbine blade, Appl. Therm. Eng. 110 (2017) 504−520.
[16] X.J. Wang, G.L. Liao, F. Zhang, J. Li, Numerical investigation on the steady and unsteady flow characteristics of rim seal for the first stage in gas turbine, Appl. Therm. Eng. 99 (2016) 11−22.
[17] M. Ghasemian, M. Princevac, Y.W. Kim, H.D. Hamm, Numerical modeling of hot gas ingestion into the rotor-stator disk cavities of a subscale 1.5-stage axial gas turbine, Int. J. Heat Mass Tran. 130 (2019) 1016−1031.
[18] J.A. Scobie, R. Teuber, Y.S. Li, C.M. Sangan, M. Wilson, G.D. Lock, Design of an improved turbine rim-seal, ASME J. Eng. Gas Turbines Power 138 (2016) 022503-1−022503-10.
[19] F. Gao, J.W. Chew, P.F. Beard, D. Amirante, N.J. Hills, Large-eddy simulation of unsteady turbine rim sealing flows, Int. J. Heat Fluid Flow 70 (2018) 160−170.

[20] L.M. Song, P.Y. Zhu, J. Li, Z.P. Feng, Effects of location and profile of upstream slot on the endwall aerothermal performance of a gas turbine blade, Appl. Therm. Eng. 140 (2018) 637−656.
[21] I. Popovic, H.P. Hodson, The effects of a parametric variation of the rim seal geometry on the interaction between hub leakage and mainstream flows in high pressure turbines, ASME J. Eng. Gas Turbines Power 135 (2013) 112501-1−112501-11.
[22] M. Fiore, N. Gourdain, J.-F. Boussuge, E. Lippinois, Description of the flow in a linear cascade with an upstream cavity, part 1: influence of turbulence, Comput. Fluids 199 (2020) 104361.
[23] K.Y. Zhang, Z.G. Li, J. Li, Effect of gas turbine endwall misalignment with slashface leakage on the blade endwall aerothermal performance, Int. J. Heat Mass Tran. 131 (2019) 1247−1259.
[24] J. Cui, P. Tucker, Numerical study of purge and secondary flows in a low-pressure turbine, ASME J. Turbomachinery 139 (2017) 021007-1−021007-10.
[25] X.Y. Jia, H. Zhang, Q. Zheng, Numerical investigation on the effect of hot running rim seal clearance on hot gas ingestion into rotor-stator system, Appl. Therm. Eng. 152 (2019) 79−91.
[26] M. Fiore, N. Gourdain, J.-F. Boussuge, E. lippinois, Delineating loss sources within a linear cascade with upstream cavity and purge flow, ASME J. Turbomachinery 141 (2019) 091008-1−091008-13.
[27] N. Liamis, J.-M. Duboué, CFD Analysis of High Pressure Turbines, ASME Paper No. 98-GT-453, 1998.
[28] J.-M. Duboué, N. Liamis, L. Pate, Recent Advances in Aerothermal Turbine Design and Analysis, AIAA Paper No. 2000-3355, 2000.
[29] T. Arts, J.-M. Duboué, J. Rollin, Aerothermal performance measurements and analysis of a two-dimensional high turning rotor blade, Transactions of the ASME 120 (1998) 494−499.
[30] Z.Q. Zhang, W.C. Tao, Y.K. Song, Z.J. Lei, Y.F. Zhang, The Sealing Efficiency and Interaction between Purge Flow and Mainstream Flow for Novel Rim Seal Configurations, GPPS Paper No. 2019-0175, 2019.
[31] R.J. Goldstein, R.A. Spores, Turbulent transport on the endwall in the region between adjacent turbine blades, ASME J. Heat Transfer 110 (1988) 862−869.
[32] ANSYS CFX-Solver Theory Guide, ANSYS-Inc, 2011.